

# High-efficiency mid-infrared InGaAs/InP arrayed waveguide gratings

TUSHAR SANJAY KARNIK,<sup>1,3,\*</sup>  KHOI PHUONG DAO,<sup>1,3</sup>   
QINGYANG DU,<sup>1,3</sup>  LAURENT DIEHL,<sup>2</sup> CHRISTIAN PFLÜGL,<sup>2</sup>  
DARYOOSH VAKHSHOORI,<sup>2</sup> AND JUEJUN HU<sup>1</sup>

<sup>1</sup>*Department of Materials Science & Engineering, Massachusetts Institute of Technology, Cambridge, Massachusetts 02139, USA*

<sup>2</sup>*Pendar Technologies, LLC, Cambridge, Massachusetts 02138, USA*

<sup>3</sup>*Contributed equally to this work.*

\*[tkarnik@mit.edu](mailto:tkarnik@mit.edu)

**Abstract:** Photonic integrated circuits and mid-infrared quantum cascade lasers have attracted significant attention over the years because of the numerous applications enabled by these compact semiconductor chips. In this paper, we demonstrate low loss passive waveguides and highly efficient arrayed waveguide gratings that can be used, for example, to beam combine infrared (IR) laser arrays. The waveguide structure used consists of an In<sub>0.53</sub>Ga<sub>0.47</sub>As core and InP cladding layers. This material system was chosen because of its compatibility with future monolithic integration with quantum cascade lasers. Different photonic circuits were fabricated using standard semiconductor processes, and experiments conducted with these chips demonstrated low-loss waveguides with an estimated propagation loss of ~ 1.2 dB/cm as well as micro-ring resonators with an intrinsic Q-factor of 174,000. Arrayed waveguide gratings operating in the 5.15–5.34 μm range feature low insertion loss and non-uniformity of ~ 0.9 dB and ~ 0.6 dB, respectively. The demonstration of the present photonic circuits paves the path toward monolithic fabrication of compact infrared light sources with advanced functionalities beneficial to many chemical sensing and high-power applications.

© 2023 Optica Publishing Group under the terms of the [Optica Open Access Publishing Agreement](#)

## 1. Introduction

Leveraging photonic integrated circuits (PICs) technology is particularly attractive as this can result in a significant reduction in size, weight, power, and cost (SWaP-C) of infrared (IR) subsystems critical to many important applications ranging from spectroscopy [1–4], sensing [5–9], nonlinear optics [10–13], laser surgery [14], and infrared countermeasures [15]. Quantum cascade lasers (QCLs) are the ideal light sources for the integration with mid-IR PICs, and typically consist of epitaxial III-V semiconductor layers grown on an indium phosphide (InP) substrate [16]. Arrays of QCLs are of particular interest, for example, for broadband chemical sensing [17] or to increase the output power of infrared laser sources well beyond what can be achieved with a single emitter. However, most applications require a single output with good beam quality [18], and therefore various strategies to spatially overlap the beams from an array of laser sources have been devised. Open loop wavelength beam combining (WBC) is a well-known method to achieve this goal but requires single-mode lasers operating at different wavelengths [19]. WBC of distributed feedback (DFB) QCL arrays has been successfully developed using external optics [20,21]. Building on those past accomplishments, the monolithic beam-combining of QCL arrays enabled by the present work aims at significantly reducing the footprint and ruggedness of mid-IR WBC laser sources. The level of integration pursued also eliminates the labor-intensive alignment procedures required when using external optics since the waveguides are lithographically defined, therefore leveraging the scalability of semiconductor technology to reduce the cost of the laser sources.

Tremendous development efforts have been made in the past 30 years to mature PIC technology for the telecom industry in particular. Arrayed waveguide gratings (AWG) [22] and echelle gratings (EG) [23] are the commonly used (de)multiplexer devices for WBC PICs due to their small footprint and passive nature. Many research groups have demonstrated AWG/EG working in the visible and near-IR with low insertion losses, typically on the order of 0.5 to 5 dB [24–28]. Leveraging these advances to develop mid-IR AWGs/EGs is however not straightforward as the standard silicon-on-insulator (SOI) waveguides material technology used for most NIR or visible PICs suffers from optical absorption beyond  $4\ \mu\text{m}$  wavelengths unless large-core waveguides are used [1,29–31] or a germanium-on-silicon [32] platform is adopted instead.

Alternatively, heterogeneous integration of QCLs with silicon-based beam combining chips [33–35] can reduce the overall cost of such devices. However, it increases fabrication complexity and requires efficient coupling designs to transfer light from one material platform to another. Monolithic fabrication of QCLs and passive waveguides is a more desirable approach to realizing such integration [36]. Recent fabrication advances and the ability to have low doping

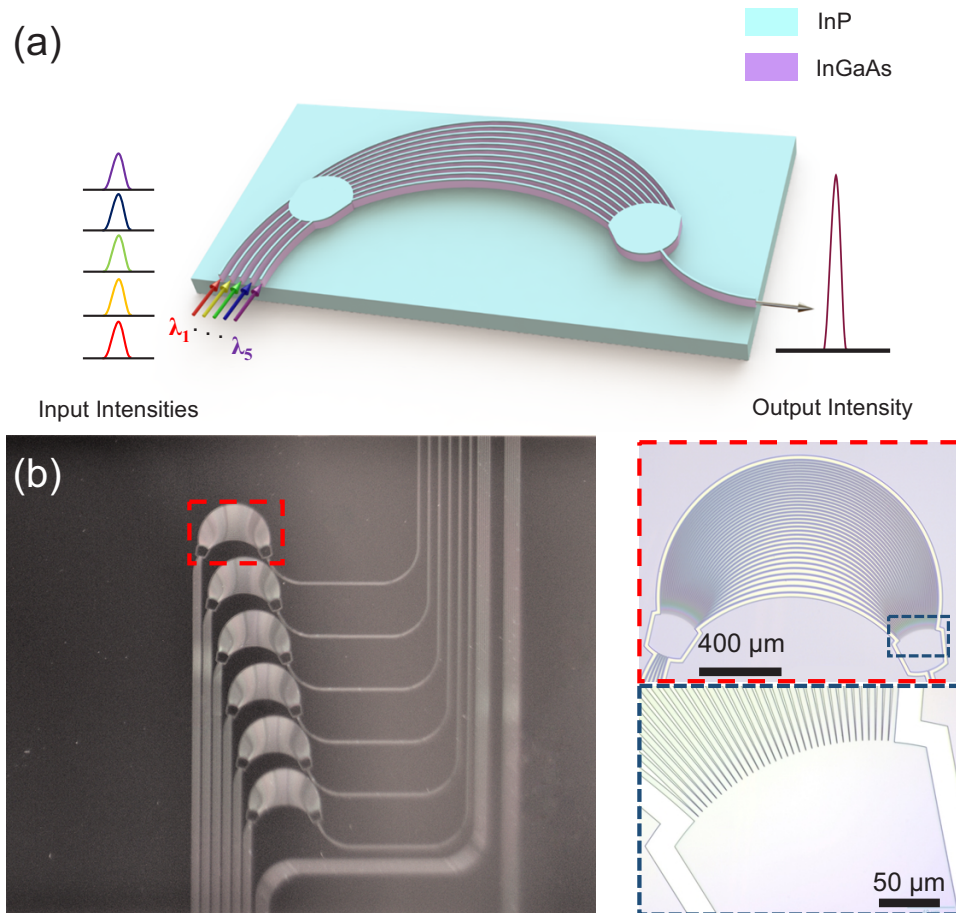


**Fig. 1.** (a) Schematic of a  $5 \times 1$  arrayed waveguide grating (AWG) multiplexer that can be used to wavelength beam combine 5 element MWIR laser array. The transmission of the AWG is centered around  $\lambda \approx 5.2\ \mu\text{m}$  by design. (b) Photograph of one of the photonic integrated chips fabricated and tested in this work. This PIC consists of six  $5 \times 1$  AWGs and reference waveguides. The insets show microscope images of a single AWG (red square) and the star coupler (blue square).

concentrations have reduced the propagation losses of semiconductor waveguides to the same ballpark as silicon waveguides, making it possible to have high-performance components fabricated on InP substrate. Many recent publications reported the demonstration of low-loss III-V [37–40] waveguides and their integration with QCLs [41–44]. Although InP-based AWG/EG's have been demonstrated for the mid-IR [40,45,46], their performance has not been comparable to silicon/germanium-based ones with relatively high insertion losses of 6 to 20 dB. A robust solution for efficient mid-IR on-chip beam combining is therefore still missing.

This work presents the fabrication of low-loss InGaAs/InP waveguides for operation in the mid-IR regime. The waveguides are 1.7  $\mu\text{m}$  tall and 5.2  $\mu\text{m}$  wide to support the fundamental transverse magnetic ( $\text{TM}_{00}$ ) mode, best suited for integration with QCLs. We determined the propagation losses in these waveguides by testing two different types of samples and using the Fabry-Perot (FP) fringe contrast [48] and ring resonator [38] methods. These experiments led to the demonstration of a Q-factor of over 170,000 for  $\lambda \approx 5.2 \mu\text{m}$ . To further establish the suitability of the InGaAs/InP platform for efficient WBC, we fabricated  $5 \times 1$  AWGs with 40 nm channel spacing and a 1.87  $\text{mm}^2$  footprint, as shown in Fig. 1. AWG samples based on high-efficiency designs were fabricated, and insertion losses as low as 0.9 dB were measured.

The work and results discussed here demonstrate the suitability of the InGaAs/InP platform for efficient WBC. This paves the way towards the monolithic integration of AWGs with arrays of QCLs to create high-power and/or broadband WBC laser sources for various applications. Several examples of how QCLs can be fabricated together with passive InGaAs/InP waveguides monolithically are discussed in detail in Refs. [41–44]. Moreover, the InGaAs/InP waveguides can also be used to manufacture a variety of active/passive components, enabling additional functionalities beyond beam combining.

## 2. Methods

### 2.1. Design

We designed a quasi-symmetrically cladded waveguide structure by sandwiching  $\text{In}_{0.53}\text{Ga}_{0.47}\text{As}$  core between InP upper and lower cladding layers. Because of the large index contrast between these two materials, this waveguide structure offers excellent modal confinement and enables, for example, low-loss bends with small radii of curvature while maintaining single mode operation. The waveguide geometry (width 5.2  $\mu\text{m}$ , 1.2  $\mu\text{m}$  thick  $\text{In}_{0.53}\text{Ga}_{0.47}\text{As}$  core and 0.5  $\mu\text{m}$  thick InP upper cladding) was engineered so that the  $\text{TM}_{00}$  mode supported has a similar effective refractive index (3.138) as the fundamental laser mode of a MWIR QCL ( $n_{\text{eff}} \sim 3.15$ ).

We designed two different types of photonics chips to determine the waveguide propagation losses according to two independent methods. The first method relies on the contrast of Fabry-Perot (FP) fringes [48], and samples consisting of passive waveguides with different lengths and number of bends were developed to estimate the loss in straight and curved sections separately (see Fig. 4). In addition, we fabricated ring resonators and measured their quality factor Q, from which the optical losses can be derived [38]. The samples were designed using eigenmode expansion simulations to calculate the coupling coefficients between the ring and bus waveguide. Three ring resonators were designed with a coupling length of 115  $\mu\text{m}$  and a coupling gap of 500 nm, 600 nm, and 650 nm to be close to the critical coupling condition (see Fig. 5(a)). AWG samples were also designed according to the principles discussed by M.K. Smit *et al.* [22]. The parameters listed in Table 1 were selected to obtain an AWG with the following properties: a center channel wavelength of 5.2  $\mu\text{m}$ , channel spacing of 40 nm, and free spectral range of 217.6 nm. We also added reference waveguides on the same chip to estimate the AWG on-chip transmission loss. To effectively reduce the total insertion loss of the device, the waveguide bending loss and waveguide junction loss need to be minimized. According to our finite-difference simulations, a minimum bending radius of 500  $\mu\text{m}$  is required to avoid any significant bending losses. We further added adiabatic tapers between the arrayed waveguide

and the star coupler to allow for a smooth strip-to-slab modal transition. The Lumerical MODE solver package was used for AWG design and simulations.

**Table 1. Design parameters of the AWG**

Number of input channels	5
Number of arrayed waveguides	33
Star coupler length	200 $\mu\text{m}$
Arrayed waveguides separation	200 nm
Input waveguides separation	11.2 $\mu\text{m}$
Arrayed waveguide length increment	36.4 $\mu\text{m}$
Star coupler tilt angle	20°

## 2.2. Fabrication

The waveguide core and cladding layers were grown by standard metalorganic chemical vapor deposition (MOCVD) on a semi-insulating Fe-doped InP wafer. The  $\text{In}_{0.53}\text{Ga}_{0.47}\text{As}$  stoichiometry was chosen to maintain lattice matching with the InP substrate. The stack profile consisted of a 500 nm InP upper cladding, a 1.2  $\mu\text{m}$   $\text{In}_{0.53}\text{Ga}_{0.47}\text{As}$  core, and a 500 nm InP bottom cladding on an InP substrate. Each of the layers grown was Fe doped to reduce the free-carrier concentration below  $\sim 10^{14} \text{cm}^{-3}$ , leading to negligible material absorption losses (0.015 dB/cm or lower).

The fabrication of all the PICs measured followed very similar steps. We first used plasma-enhanced chemical vapor deposition (PECVD) to deposit a 300 nm thick layer of silicon nitride on top of the InP upper cladding. The PIC layout was then patterned in ZEP520 resist using an Elionix (ELS-F125) electron beam lithography (EBL) tool and developed in ZED-N50 solution. Inductively coupled reactive ion etching (ICP-RIE) based on an  $\text{SF}_6/\text{Ar}$  gas mixture was performed to transfer the PIC pattern into the silicon nitride layer. It acted as a hard mask for the ICP-RIE etching of the InP upper cladding and InGaAs core, which was done using  $\text{BCl}_3/\text{SiCl}_4/\text{Ar}$  gas mixture while maintaining the sample at 250°C. Since this etch recipe is not selective for InGaAs and InP, we calibrated the etch rate to terminate the etch close to the interface between the InGaAs core and the InP substrate. Finally, the silicon nitride was stripped using ICP-RIE before cleaving the chips to expose the waveguide facets for edge coupling measurements. For the ring resonator measurements, we deposited anti-reflection coatings (ARC) on the cleaved facets using germanium antimony sulfide ( $\text{Ge}_{23}\text{Sb}_7\text{S}_{70}$ ) by thermal evaporation following previously established protocols [47]. The waveguide obtained had smooth and vertical sidewalls, as confirmed by the SEM images in Fig. 2(a) and (b). After the optimization of our process, well-resolved gaps as narrow as 200 nm and several microns deep can be etched with high fidelity between the arrayed waveguides at the star coupler junction, for example, as shown in Fig. 2(c).

## 2.3. Measurement

Figure 3(a) schematically illustrates our edge-coupled optical measurement setup. We used a bench-top tunable external cavity QCL (21052-MHF) from Daylight Solutions as the light source. An aspheric lens with a 0.85 numerical aperture (NA) focused the laser beam onto the input waveguide facet. The photonic chip was placed on high precision mechanical stage for accurate and stable alignment with the laser beam. The light transmitted through the waveguide was collected from the output facet by a  $\text{CaF}_2$  lens and coupled to a nitrogen-cooled indium antimonide (InSb) infrared camera. After confirming the alignment by viewing the waveguide mode image (Fig. 3(b)), we replaced the camera with a photodetector to measure the AWG transmission (Fig. 3(c)). The photodetector was connected to a Stanford Research SR810 lock-in

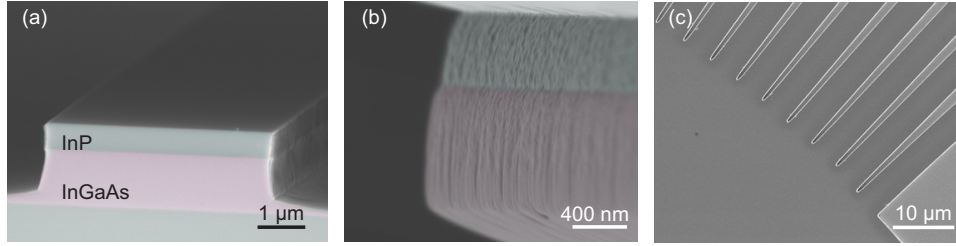


**Fig. 2.** Scanning electron microscopy (SEM) images of (a) the waveguide cross-section with added false colors; (b) waveguide sidewall with added false colors; and (c) junction between the arrayed waveguides and the star coupler.

amplifier to enhance the signal-to-noise ratio (SNR). Both the lock-in amplifier and the QCL were controlled by a computer using a LabVIEW program.

The analysis of the data obtained with the type of samples described in Fig. 4(a) was performed following the method described in [48]. As shown in Fig. 4(b) and discussed in Section 3.1, FP fringes are clearly present in the transmission data collected. The relation between the contrast of the FP fringes and waveguide propagation loss is given by Eq. (1):

$$-\alpha_s L_s - \alpha_c L_c = \ln \left( \frac{\sqrt{r} - 1}{\sqrt{r} + 1} \right) + \ln \left( \frac{1}{R} \right). \quad (1)$$

Here,  $\alpha_s$  and  $\alpha_c$  are the loss coefficients, and  $L_s$  and  $L_c$  are the length of the straight and the curved waveguide, respectively.  $r$  represents the ratio of the maximum and minimum transmission intensity (fringe contrast), and  $R$  is the reflectivity of the waveguide facets. We fabricated waveguides with varying  $L_s$  but equal  $L_c$  to obtain Eq. (2):

$$-\alpha_s L_s = \ln \left( \frac{\sqrt{r} - 1}{\sqrt{r} + 1} \right) + constant. \quad (2)$$

Thus, by plotting  $\ln \left[ \frac{(\sqrt{r} - 1)}{(\sqrt{r} + 1)} \right]$  versus  $L_s$  and measuring the slope, we estimated  $\alpha_s$ . This approach allows us to determine the waveguide loss while minimizing uncertainties associated with the unknown facet reflectivity  $R$ . We also fabricated waveguides with different number of bends and rewrote Eq. (1) as:

$$-\alpha_c L_c = \ln \left( \frac{\sqrt{r} - 1}{\sqrt{r} + 1} \right) + \alpha_s L_s + constant. \quad (3)$$

Since  $\alpha_s$  is estimated by Eq. (2), we calculated the slope by plotting  $\ln \left[ \frac{(\sqrt{r} - 1)}{(\sqrt{r} + 1)} \right] + \alpha_s L_s$  versus  $L_c$  to obtain  $\alpha_c$ .

We also estimated the propagation losses in ring resonator by measuring the loaded Q-factor of the devices described in Section 3.2 and by performing the analysis given in [49]. Equation (4) allows us to extract the propagation loss and coupling coefficient from the measured Q-factor and extinction ratio in the overcoupled regime.

$$n_g = \frac{\lambda^2}{L \cdot FSR}, \quad A = \frac{\pi n_g L}{Q \lambda}, \quad B = A \sqrt{T_{min}}, \quad \tau = \frac{1}{2} \left( -B + \sqrt{B^2 - 4(A - 1)} \right), \quad \alpha = \frac{1 - A}{\tau}. \quad (4)$$

$Q$ ,  $n_g$ ,  $L$ , and  $FSR$  are the quality factor, group index, ring circumference, and the free spectral range, respectively.  $T_{min}$  is the minimum transmission at the resonant wavelength, and  $\tau$  is defined as described in [49]. In case of undercoupling,  $\alpha$  and  $\tau$  will exchange positions in the last two expressions of Eq. (4).

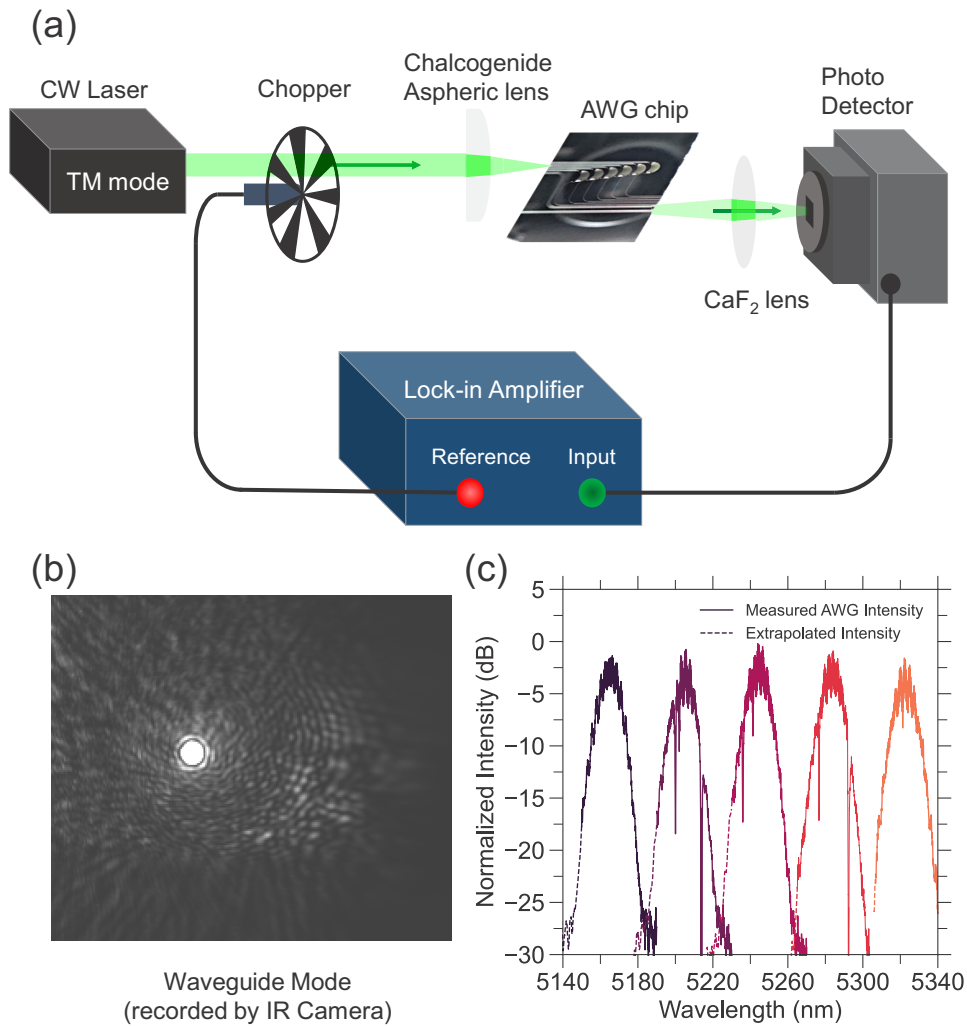


**Fig. 3.** (a) Schematic of the optical measurement setup. The alignment of the PIC under test is first done by replacing the photodetector shown here with a liquid nitrogen cooled IR camera. (b) Infrared camera image of the waveguide mode. (c) Measured AWG spectrum. The sharp dips in the transmission arise from atmospheric absorption. The dashed lines denote the extrapolation of data according to the AWG peak symmetry.

The insertion loss of AWGs is usually calculated by normalizing its measured intensity with respect to a reference waveguide. However, this leads to a significant error due to the uncertainty in edge-coupling efficiency [50]. To avoid this issue, the authors of Ref. [51] used two cascaded AWGs in a ring formation to extract their on-chip transmission independently from the edge-coupling efficiency. In our case, we inferred the efficiency of our AWG samples by comparing the contrast of FP fringes present in the AWG transmission data shown in Fig. 6 with that of a reference waveguide fabricated on the same chip (see Fig. 1(b)). Equation (5) represents the AWG electric-field transfer function where  $A$  and  $\varphi_a$  are the AWG intensity and phase, respectively.

$$G(\lambda) = \sqrt{A(\lambda)} \exp(i\varphi_a(\lambda)). \quad (5)$$

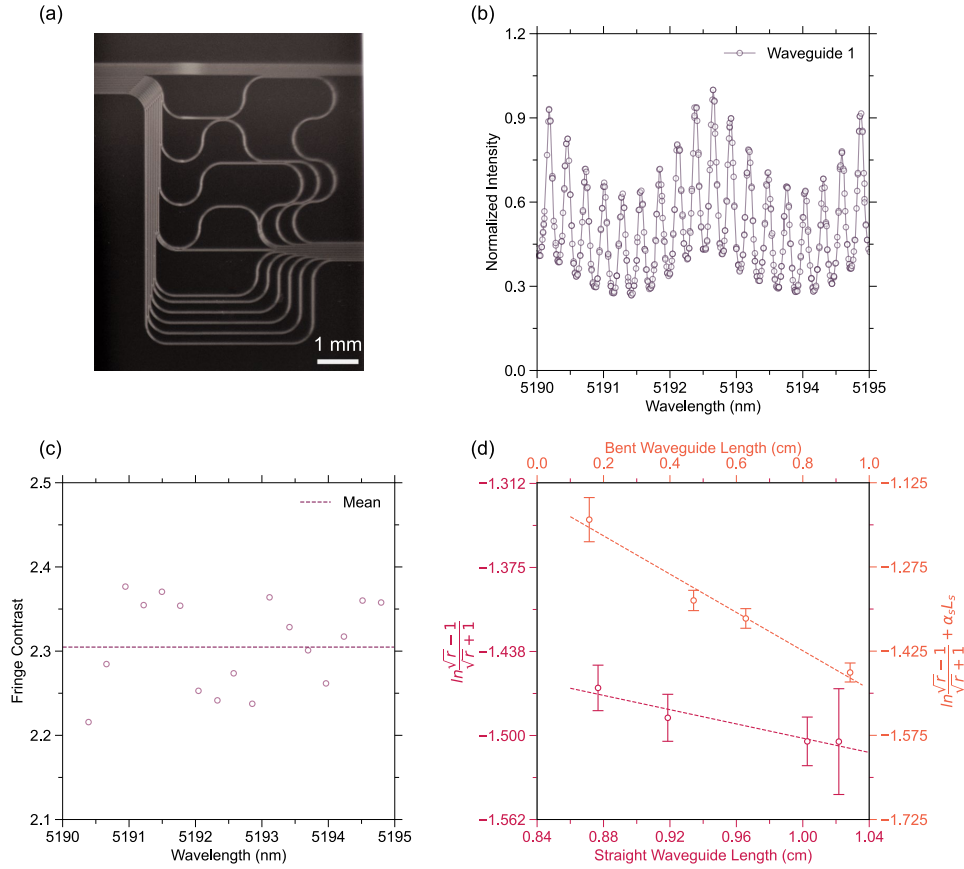


**Fig. 4.** (a) Photograph of the FP loss measurement photonic chip. (b) Intensity vs. wavelength measurement for a waveguide on the FP loss measurement chip. (c) Calculated fringe contrast for each pair of maxima and minima for the waveguide. (d) Red curve: linear fit to determine the propagation loss in straight waveguides; orange curve: linear fit to determine the propagation loss in waveguide bends.

The FP equation for a waveguide can be modified using this transfer function to model AWG transmission, and the final expression is given in Eq. (6).

$$\ln(A(\lambda)) - \alpha L' = \ln\left(\frac{\sqrt{r'(\lambda)} - 1}{\sqrt{r'(\lambda)} + 1}\right) + \ln\left(\frac{1}{R}\right). \quad (6)$$

$L'$  is the total length of the AWG input and output waveguides, and  $r'$  is the fringe contrast in the measured AWG off-chip transmission. Here we assumed that the absorption in straight and curved waveguides is approximately equal. Using the same assumption in Eq. (1) and subtracting it from Eq. (6), we get:

$$A(\lambda) = \exp(\alpha(L' - L)) \left(\frac{\sqrt{r'(\lambda)} - 1}{\sqrt{r'(\lambda)} + 1}\right) \left(\frac{\sqrt{r} + 1}{\sqrt{r} - 1}\right). \quad (7)$$

$L$  and  $r$  correspond to the length and fringe contrast in the reference waveguide, respectively. We have also assumed that the reference waveguide fringe contrast does not have a strong dependence on wavelength for the full-width half maxima (FWHM) of one AWG channel, which is valid for

our devices.  $A(\lambda)$  gives the fabricated AWG's on-chip transmission independent of the coupling efficiency.

### 3. Results and discussion

#### 3.1. Fabry-Perot loss measurement

Figure 4(b) depicts the transmission spectrum from a waveguide on the FP loss measurement chip. The high reflectivity of waveguide facets ( $\sim 0.27$ ) gives rise to strong fringe contrast (FSR  $\sim 0.28$  nm) suitable for estimating the propagation loss. Parasitic low-frequency secondary oscillations (FSR  $\sim 2.5$  nm) in the intensity signal come from the QCL power's wavelength dependence, which arises due to the FP interference in its external cavity. We eliminated these spurious power oscillations mathematically by fitting the detector signal with the FP equation provided in [48] and calculating the ratio of each consecutive pair of maxima and minima to obtain the fringe contrast  $r$  shown in Fig. 4(c). Since the fringe contrast was not constant for each pair, the mean and standard deviation was calculated for error analysis. The red curve in Fig. 4(d) shows the plot of  $\ln [(\sqrt{r} - 1) / (\sqrt{r} + 1)]$  versus  $L_s$  with error bars and linear fit for the waveguides with the same number of bends. The propagation loss in the straight waveguide was found to be  $1.15 \pm 0.47$  dB/cm. From the slope of the orange curve in (d), the value of  $\alpha_c$  can be deduced according to the described procedure in Section 2.3. This analysis gives a propagation loss of  $1.48 \pm 0.23$  dB/cm in the bent waveguide, which implies a loss of only  $0.074 \pm 0.012$  dB per  $500 \mu\text{m}$  radius bend.

#### 3.2. Ring resonator loss measurement

Ring resonators were fabricated as an alternative means to assess the waveguide loss, which can re-confirm our result measured by FP while having less susceptibility to fabrication error due to its small footprint. We deposited ARC on the facets of the ring resonator chip to mitigate FP interference which distorts the resonant peaks related to the rings. The resonator signal was normalized to the maximum intensity, and a similar procedure to the one discussed in Section 3.1 was followed to eliminate the parasitic wavelength dependence of the laser power. According to Fig. 5(b), the peak extinction increased with increasing coupling gap from 500 nm to 650 nm, indicating operation in the over-coupled regime. The peaks of the ring resonators can be adequately fitted using Lorentz functions as shown in Fig. 5(c). The propagation loss was calculated to be  $1.17 \pm 0.06$  dB/cm, consistent with the conclusions of our FP measurements described in Section 3.1. The result corresponds to an intrinsic quality factor of  $174,000 \pm 8,000$ .

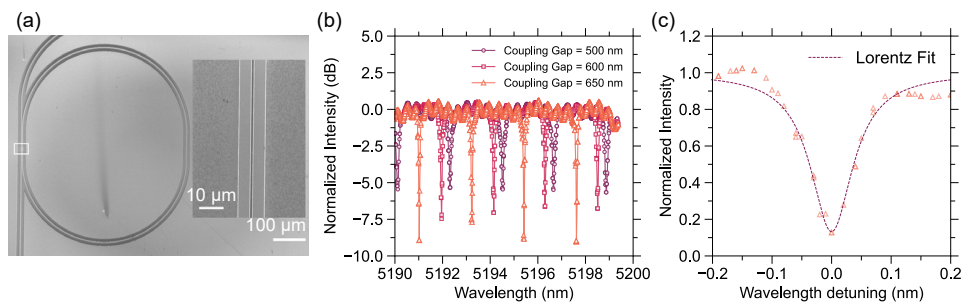


**Fig. 5.** (a) SEM image of a ring resonator with  $500 \mu\text{m}$  coupling gap with inset showing the coupling region. (b) Normalized intensity vs. wavelength scan of the ring resonator with coupling gap equal to 500 (purple), 600 (red), and 650 nm (orange). (c) A resonant peak of the 650 nm coupling gap ring resonator fitted with a Lorentz function.

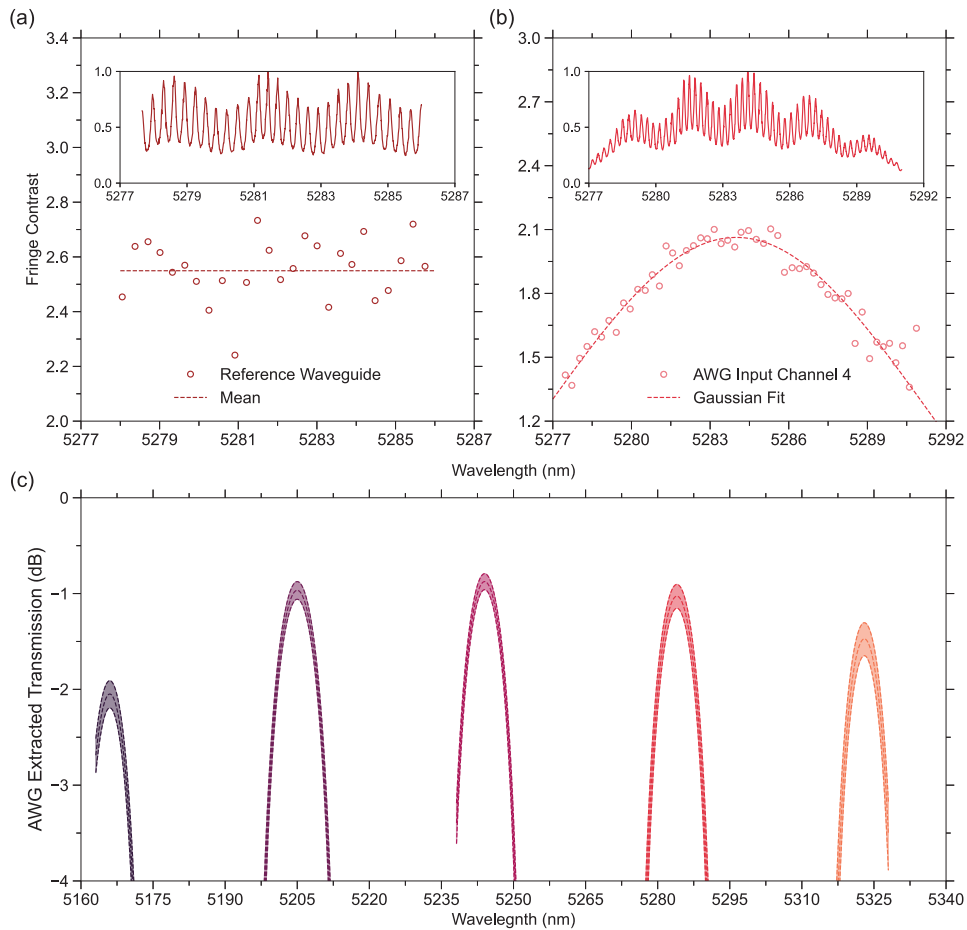


**Fig. 6.** (a) AWG reference waveguide fringe contrast vs. wavelength with inset showing the spectrum. (b) AWG fringe contrast vs. wavelength for the input channel centered at  $\sim 5284$  nm with inset showing the measured spectrum. (c) Extracted AWG transmission vs. wavelength for all input channels where shaded region represents the error in our calculation method.

To the best of our knowledge, this is the highest Q-factor reported in mid-IR III-V semiconductor resonators.

### 3.3. Arrayed waveguide grating performance

A five-by-one AWG was fabricated to demonstrate that efficient WBC can be achieved. The five input channels are numbered in the ascending order of their peak wavelengths. We coupled the beam of the external cavity QCL used in our setup (Fig. 3(a)) into each input channel and tuned the laser wavelength to obtain the full AWG spectrum. Since the sample tested was cleaved but no ARCs were deposited, FP fringes were clearly observable in the detector signal. A slow parasitic oscillation due to the QCL was again present in the collected data and was eliminated following the procedure described in Section 3.1. The fringe contrast of the reference waveguide and input channel 4 centering at  $\sim 5284$  nm is shown in Fig. 6(a) and (b), respectively. The Gaussian fit was used to infer the wavelength dependence of each input channel's fringe contrast. The AWG on-chip transmission is extracted from Eq. (7) and plotted in Fig. 6(c), where the

shaded region represents the estimated error bar. We calculated this error from the uncertainty in measuring the fringe contrast, and more details can be found in the [Appendix](#). The transmission of input channel 1 is lower than that of channel 5 by approximately 0.6 dB. We account for this difference to fabrication defect in the input waveguide of channel 1. The channel crosstalk could not be measured directly as its signal strength was below the noise floor of the photodetector. However, we can confirm that its value is below -26 dB as observed in Fig. 3(c). The central channel wavelength was measured to be 5.244  $\mu\text{m}$  instead of the design value of 5.200  $\mu\text{m}$ , most likely due to a difference in the simulated and actual value of the waveguide effective indices. AWG insertion loss and non-uniformity were estimated to be  $0.88 \pm 0.08$  dB and  $0.60 \pm 0.18$  dB, respectively. These are the lowest reported values for this wavelength range to the best of our knowledge.

#### 4. Conclusion

This paper describes the design, fabrication, and optical characterization of low-loss InGaAs/InP PICs operating in the mid-IR and the experimental results are summarized in Table 2. We measured the waveguide propagation loss by FP fringe contrast and ring resonator Q-factor. These losses are comparable to other mid-IR waveguides as shown in the [Appendix Table 3](#), and could be further reduced by post-fabrication acid treatment, as mentioned in [37]. Our results of the AWG characterization indicate a potential for developing high-efficiency beam combining with III-V semiconductor materials. The ability to further reduce the gap between arrayed waveguides at the star coupler junction could lower the insertion loss and non-uniformity. Our work demonstrated a promising solution for the monolithic integration of AWGs with QCLs to achieve efficient WBC for example. The low-loss platform and fabrication technology developed are also equally applicable to other III-V based PICs enabling new functionalities.

**Table 2. Summary of experimental results**

Measured Property	Value
Straight waveguide loss (FP method)	$1.15 \pm 0.47$ dB/cm
Curved waveguide loss (FP method)	$1.48 \pm 0.23$ dB/cm
Ring resonator loss	$1.17 \pm 0.06$ dB/cm
Intrinsic Q-factor	$174,000 \pm 8,000$
AWG insertion loss	$0.88 \pm 0.08$ dB
AWG non-uniformity	$0.60 \pm 0.18$ dB

#### Appendix

The error in our estimation of the AWG on-chip transmission ( $A$ ) arises from the uncertainty in the fringe contrast measurement for the reference waveguide ( $r$ ) and AWG input channels ( $r'$ ). In a function dependent on two variables, the error dependence on the variables is given by:

$$\sigma_{f(x,y)}^2 = \left( \frac{\partial f(x,y)}{\partial x} \right)_y^2 \sigma_x^2 + \left( \frac{\partial f(x,y)}{\partial y} \right)_x^2 \sigma_y^2. \quad (8)$$

Since  $L'-L$  and  $\alpha$  in Eq. (7) are 478  $\mu\text{m}$  and  $0.272 \text{ cm}^{-1}$ , respectively, the exponential term is close to unity, and the error in  $\alpha$  will not significantly contribute to the error in  $A$ . Replacing

$f(x,y)$  with  $A(r',r)$  in Eq. (8), we obtain the relation between  $\sigma_A$ ,  $\sigma_{r'}$ , and  $\sigma_r$ .

$$\sigma_A^2(\lambda) = \left( \frac{1}{(\sqrt{r'(\lambda)} + 1)^2 \sqrt{r'(\lambda)}} \frac{\sqrt{r} + 1}{\sqrt{r} - 1} \right)^2 \sigma_{r'}^2 + \left( \frac{1}{(\sqrt{r} + 1)^2 \sqrt{r}} \frac{\sqrt{r'(\lambda)} + 1}{\sqrt{r'(\lambda)} - 1} \right)^2 \sigma_r^2. \quad (9)$$

$\sigma_r$  is the standard deviation of the reference waveguide fringe contrast, and  $\sigma_{r'}$  is the RMSE of the Gaussian fit used to model the wavelength dependence of  $r'$ .

**Table 3. Comparison of propagation loss with other works**

Waveguide material	Wavelength ( $\mu\text{m}$ )	Bend radius ( $\mu\text{m}$ )	Propagation loss (dB/cm)
SOI [31]	3.8	150	0.20
Suspended Si [52]	3.8	15.7	0.82
Silicon on sapphire [53]	4.5	60	0.74
Ge on SOI [54]	3.8	N.A.	0.6
Ge on Si [55]	5.8	115	2.50
InGaAs/InP [37]	5.2	300	0.50
InGaAs/InP (This work)	5.2	500	1.17

**Funding.** Naval Sea Systems Command (N68335-20-C-0845).

**Acknowledgments.** The authors acknowledge characterization facility support provided by the Materials Research Laboratory at Massachusetts Institute of Technology (MIT) and fabrication facility support by MIT.Nano. Any opinions, findings and conclusions or recommendations expressed in this material are those of the author(s) and do not necessarily reflect the views of Naval Sea Systems Command.

**Disclosures.** The authors declare no conflicts of interest.

**Data availability.** Data underlying the results presented in this paper are not publicly available at this time but may be obtained from the authors upon reasonable request.

## References

1. M. Muneeb, X. Chen, P. Verheyen, G. Lepage, S. Pathak, E. Ryckeboer, A. Malik, B. Kuyken, M. Nedeljkovic, J. van Campenhout, G. Z. Mashanovich, and G. Roelkens, "Demonstration of Silicon-on-insulator mid-infrared spectrometers operating at 3.8 $\mu\text{m}$ ," *Opt. Express* **21**(10), 11659–11669 (2013).
2. M. Muneeb, A. Vasiliev, A. Ruocco, A. Malik, H. Chen, M. Nedeljkovic, J. S. Penades, L. Cerutti, J. B. Rodriguez, G. Z. Mashanovich, M. K. Smit, E. Tourni, and G. Roelkens, "III-V-on-silicon integrated micro - spectrometer for the 3  $\mu\text{m}$  wavelength range," *Opt. Express* **24**(9), 9465–9472 (2016).
3. M. Yu, Y. Okawachi, A. G. Griffith, N. Picqué, M. Lipson, and A. L. Gaeta, "Silicon-chip-based mid-infrared dual-comb spectroscopy," *Nat. Commun.* **9**(1), 1–6 (2018).
4. D. Kita, H. Lin, A. Agarwal, K. Richardson, I. Luginov, T. Gu, and J. Hu, "On-chip infrared spectroscopic sensing: redefining the benefits of scaling," *IEEE J. Sel. Top. Quantum Electron.* **23**(2), 5900110 (2017).
5. V. Singh, P. T. Lin, and N. Patel, *et al.*, "Mid-infrared materials and devices on a Si platform for optical sensing," *Sci. Technol. Adv. Mater.* **15**(1), 014603 (2014).
6. P. Ma, D.-Y. Choi, Y. Yu, X. Gai, Z. Yang, S. Debbarma, S. Madden, and B. Luther-Davies, "Low-loss chalcogenide waveguides for chemical sensing in the mid-infrared," *Opt. Express* **21**(24), 29927–29937 (2013).
7. Z. Han, P. Lin, V. Singh, L. Kimerling, J. Hu, K. Richardson, A. Agarwal, and D. T. H. Tan, "On-chip mid-infrared gas detection using chalcogenide glass waveguide," *Appl. Phys. Lett.* **108**(14), 141106 (2016).
8. Y. Chen, H. Lin, J. Hu, and M. Li, "Heterogeneously integrated silicon photonics for the mid-infrared and spectroscopic sensing," *ACS Nano* **8**(7), 6955–6961 (2014).
9. P. Su, Z. Han, D. Kita, P. Becla, H. Lin, S. Deckoff-Jones, K. Richardson, L. C. Kimerling, J. Hu, and A. Agarwal, "Monolithic on-chip mid-IR methane gas sensor with waveguide-integrated detector," *Appl. Phys. Lett.* **114**(5), 051103 (2019).
10. J. Rong Ong, *Nanophotonics and Plasmonics* (CRC Press, 2017), pp. 275–304.
11. Q. Du, Z. Luo, H. Zhong, Y. Zhang, Y. Huang, T. Du, W. Zhang, T. Gu, and J. Hu, "Chip-scale broadband spectroscopic chemical sensing using an integrated supercontinuum source in a chalcogenide glass waveguide," *Photonics Res.* **6**(6), 506–510 (2018).

12. Y. Yu, X. Gai, P. Ma, D. Y. Choi, Z. Yang, R. Wang, S. Debarma, S. J. Madden, and B. Luther-Davies, "A broadband, quasi-continuous, mid-infrared supercontinuum generated in a chalcogenide glass waveguide," *Laser Photonics Rev.* **8**(5), 792–798 (2014).
13. M. Montesinos-Ballester, C. Lafforgue, J. Frigerio, A. Ballabio, V. Vakarin, Q. Liu, J. M. Ramirez, X. le Roux, D. Bouville, A. Barzaghi, C. Alonso-Ramos, L. Vivien, G. Isella, and D. Marris-Morini, "On-Chip Mid-Infrared Supercontinuum Generation from 3 to 13  $\mu\text{m}$  Wavelength," *ACS Photonics* **7**(12), 3423–3429 (2020).
14. P. I. Abramov, E. V. Kuznetsov, L. A. Skvortsov, and M. I. Skvortsova, "Quantum-Cascade Lasers in Medicine and Biology (Review)," *J. Appl. Spectrosc.* **86**(1), 1–26 (2019).
15. D. H. Titterton, "A review of the development of optical countermeasures," *Proc. SPIE* **5615**, 1–15 (2004).
16. J. Faist, F. Capasso, D. L. Sivco, C. Sirtori, A. L. Hutchinson, and A. Y. Cho, "Quantum Cascade Laser," *Science* **264**(5158), 553–556 (1994).
17. B. G. Lee, M. A. Belkin, R. Audet, J. MacArthur, L. Diehl, C. Pflugl, D. Oakley, D. Chapman, A. Napoleone, D. Bour, S. Corzine, G. Hoffer, J. Faist, and F. Capasso, "Widely tunable single-mode quantum cascade laser source for mid-infrared spectroscopy," *Appl. Phys. Lett.* **91**(23), 231101 (2007).
18. T. Y. Fan, "Laser beam combining for high-power, high-radiance sources," *IEEE J. Select. Topics Quantum Electron.* **11**(3), 567–577 (2005).
19. A. Sanchez-Rubio, Y. Fan, S. J. Augst, A. K. Goyal, K. J. Creedon, J. T. Gopinath, V. Daneu, B. Chann, and R. Huang, "Wavelength Beam Combining for Power and Brightness Scaling of Laser Systems," *Lincoln Laboratory Journal* **20**(2), 52–66 (2014).
20. B. G. Lee, J. Kinsky, A. K. Goyal, C. Pflugl, L. Diehl, M. A. Belkin, A. Sanchez, and F. Capasso, "Beam combining of quantum cascade laser arrays," *Opt. Express* **17**(18), 16216–16224 (2009).
21. P. Rauter and F. Capasso, "Multi-wavelength quantum cascade laser arrays," *Laser Photonics Rev.* **9**(5), 452–477 (2015).
22. M. K. Smit and C. V. Dam, "PHASAR-based WDM-devices: Principles, design and applications," *IEEE J. Select. Topics Quantum Electron.* **2**(2), 236–250 (1996).
23. D. Chowdhury, "Design of low-loss and polarization-insensitive reflection grating-based planar demultiplexers," *IEEE J. Select. Topics Quantum Electron.* **6**(2), 233–239 (2000).
24. J. Zou, Z. Le, J. Hu, and J.-J. Hu, "Performance improvement for silicon-based arrayed waveguide grating router," *Opt. Express* **25**(9), 9963–9973 (2017).
25. D. Dai, Z. Wang, J. F. Bauters, M.-C. Tien, M. J. R. Heck, D. J. Blumenthal, and J. E. Bowers, "Low-loss  $\text{Si}_3\text{N}_4$  arrayed-waveguide grating (de)multiplexer using nano-core optical waveguides," *Opt. Express* **19**(15), 14130–14136 (2011).
26. D. Feng, N.-N. Feng, C.-C. Kung, H. Liang, W. Qian, J. Fong, B. Jonathan Luff, and M. Asghari, "Compact single-chip VMUX/DEMUX on the silicon-on-insulator platform," *Opt. Express* **19**(7), 6125–6130 (2011).
27. E. J. Stanton, A. Spott, M. L. Davenport, N. Volet, and J. E. Bowers, "Low-loss arrayed waveguide grating at 760 nm," *Opt. Lett.* **41**(8), 1785–1788 (2016).
28. D. Martens, A. Z. Subramanian, S. Pathak, M. Vanslebrouck, P. Bienstman, W. Bogaerts, and R. G. Baets, "Compact silicon nitride arrayed waveguide gratings for very near-infrared wavelengths," *IEEE Photonics Technol. Lett.* **27**(2), 137–140 (2015).
29. A. Malik, M. Muneeb, S. Radosavljevic, M. Nedeljkovic, J. S. Penades, G. Mashanovich, Y. Shimura, G. Lepage, P. Verheyen, W. Vanherle, T. van Opstal, R. Loo, J. van Campenhout, and G. Roelkens, "Silicon-based Photonic Integrated Circuits for the Mid-infrared," *Procedia Eng.* **140**, 144–151 (2016).
30. A. Malik, A. Spott, Y. Wang, E. J. Stanton, J. Peters, and J. E. Bowers, "High resolution, high channel count mid-infrared arrayed waveguide gratings in silicon," *Opt. Lett.* **45**(16), 4551–4554 (2020).
31. S. A. Miller, M. Yu, X. Ji, A. G. Griffith, J. Cardenas, A. L. Gaeta, and M. Lipson, "Low-loss silicon platform for broadband mid-infrared photonics," *Optica* **4**(7), 707–712 (2017).
32. A. Malik, E. J. Stanton, J. Liu, A. Spott, and J. E. Bowers, "High Performance  $7 \times 8$  Ge-on-Si Arrayed Waveguide Gratings for the Midinfrared," *IEEE J. Sel. Top. Quantum Electron.* **24**(6), 8300108 (2018).
33. E. J. Stanton, A. Spott, N. Volet, M. L. Davenport, and J. E. Bowers, "High-brightness lasers on silicon by beam combining [Invited]," *Proc. SPIE* **10108**, 101080K (2017).
34. S. Zeng, X. Zhao, Y. Zhu, L. Sweatt, and L. Zhu, "Watt-level beam combined diode laser systems in a chip-scale hybrid photonic platform," *Opt. Express* **30**(13), 23815–23827 (2022).
35. A. Spott, J. Peters, M. L. Davenport, E. J. Stanton, C. D. Merritt, W. W. Bewley, I. Vurgaftman, C. S. Kim, J. R. Meyer, J. Kirch, L. J. Mawst, D. Botez, and J. E. Bowers, "Quantum cascade laser on silicon," *Optica* **3**(5), 545–551 (2016).
36. H. Lin, C. S. Kim, L. Li, M. Kim, W. W. Bewley, C. D. Merritt, C. L. Canedy, I. Vurgaftman, A. Agarwal, K. Richardson, J. Hu, and J. R. Meyer, "Monolithic chalcogenide glass waveguide integrated interband cascaded laser," *Opt. Mater. Express* **11**(9), 2869–2876 (2021).
37. K. Zhang, G. Böhm, and M. A. Belkin, "Mid-infrared microring resonators and optical waveguides on an InP platform," *Appl. Phys. Lett.* **120**(6), 061106 (2022).
38. C. Ciminelli, F. Dell'Olio, M. N. Armenise, F. M. Soares, and W. Passenberg, "High performance InP ring resonator for new generation monolithically integrated optical gyroscopes," *Opt. Express* **21**(1), 556–564 (2013).

39. D. D'Agostino, G. Carnicella, C. Ciminelli, P. Thijs, P. J. Veldhoven, H. Ambrosius, and M. Smit, "Low-loss passive waveguides in a generic InP foundry process via local diffusion of zinc," *Opt. Express* **23**(19), 25143–25157 (2015).
40. C. Gilles, L. Jorge Orbe, G. Carpintero, G. Maisons, and M. Carras, "Mid-infrared wavelength multiplexer in InGaAs/InP waveguides using a Rowland circle grating," *Opt. Express* **23**(16), 20288–20296 (2015).
41. C. Gilles, L. Orbe, G. Carpintero, J. Abautret, G. Maisons, A. C. Gilles, L. J. Orbe, and M. Carras, "Monolithic integration of a quantum cascade laser array and an echelle grating multiplexer for widely tunable mid-infrared sources," *Proc. SPIE* **9767**, 97671R (2016).
42. S. Jung, D. Palaferri, K. Zhang, F. Xie, Y. Okuno, C. Pinzone, K. Lascola, and M. A. Belkin, "Homogeneous photonic integration of mid-infrared quantum cascade lasers with low-loss passive waveguides on an InP platform," *Optica* **6**(8), 1023–1030 (2019).
43. R. Wang, P. Täschler, Z. Wang, E. Gini, M. Beck, and J. Faist, "Monolithic Integration of Mid-Infrared Quantum Cascade Lasers and Frequency Combs with Passive Waveguides," *ACS Photonics* **9**(2), 426–431 (2022).
44. J. Montoya, C. Wang, A. Goyal, K. Creedon, M. Connors, J. Daulton, J. Donnelly, L. Missaggia, C. Aleshire, A. Sanchez-Rubio, and W. Herzog, "Integration of quantum cascade lasers and passive waveguides," *Appl. Phys. Lett.* **107**(3), 031110 (2015).
45. J. Bolk, H. Ambrosius, R. Stabile, S. Latkowski, X. Leijtens, E. Bitincka, L. Augustin, D. Marsan, J. Darracq, and K. Williams, "Deep UV Lithography Process in Generic InP Integration for Arrayed Waveguide Gratings," *IEEE Photonics Technol. Lett.* **30**(13), 1222–1225 (2018).
46. Y. Yoshikuni, "Semiconductor arrayed waveguide gratings for photonic integrated devices," *IEEE J. Select. Topics Quantum Electron.* **8**(6), 1102–1114 (2002).
47. J. Hu, V. Tarasov, A. Agarwal, L. Kimerling, N. Carlie, L. Petit, and K. Richardson, "Fabrication and testing of planar chalcogenide waveguide integrated microfluidic sensor," *Opt. Express* **15**(5), 2307–2314 (2007).
48. S. Taebi, M. Khorasaninejad, and S. S. Saini, "Modified Fabry-Perot interferometric method for waveguide loss measurement," *Appl. Opt.* **47**(35), 6625–6630 (2008).
49. A. Yariv, "Universal relations for coupling of optical power between microresonators and dielectric waveguides," *Electron. Lett.* **36**(4), 321–322 (2000).
50. G. Tittelbach, B. Richter, and W. Karthe, "Comparison of three transmission methods for integrated optical waveguide propagation loss measurement," *Pure Appl. Opt.* **2**(6), 683–700 (1993).
51. E. J. Stanton, N. Volet, and J. E. Bowers, "Low-loss demonstration and refined characterization of silicon arrayed waveguide gratings in the near-infrared," *Opt. Express* **25**(24), 30651–30663 (2017).
52. J. S. Penades, A. Ortega-Moñux, M. Nedeljkovic, J. G. Wangüemert-Pérez, R. Halir, A. Z. Khokhar, C. Alonso-Ramos, Z. Qu, I. Molina-Fernández, P. Cheben, and G. Z. Mashanovich, "Suspended silicon mid-infrared waveguide devices with subwavelength grating metamaterial cladding," *Opt. Express* **24**(20), 22908–22916 (2016).
53. R. Shankar, I. Bulu, and M. Loncar, "Integrated high-quality factor silicon-on-sapphire ring resonators for the mid-infrared," *Appl. Phys. Lett.* **102**(5), 051108 (2013).
54. M. Nedeljkovic, J. S. Penadés, C. J. Mitchell, A. Z. Khokhar, S. Stankovic, T. D. Bucio, C. G. Littlejohns, F. Y. Gardes, and G. Z. Mashanovich, "Surface-Grating-Coupled Low-Loss Ge-on-Si Rib Waveguides and Multimode Interferometers," *IEEE Photonics Technol. Lett.* **27**(10), 1040–1043 (2015).
55. Y. Chang, V. Paeder, L. Hvozdar, J. Hartmann, and H. P. Herzig, "Low-loss germanium strip waveguides on silicon for the mid-infrared," *Opt. Lett.* **37**(14), 2883–2885 (2012).